Bioactive Materials 6 (2021) 123–136

Contents lists available at ScienceDirect

Bioactive Materials

journal homepage: http://www.keaipublishing.com/biomat

Nanotherapeutics for regeneration of degenerated tissue infected by bacteria through the multiple delivery of bioactive ions and growth factor with antibacterial/angiogenic and osteogenic/odontogenic capacity

Ahmed El-Fiqi[a,b,c,1,*], Nandin Mandakhbayar[a,b,1], Seung Bin Jo[a], Jonathan C. Knowles[b,d,e,g], Jung-Hwan Lee[a,b,f,g,**], Hae-Won Kim[a,b,f,g,***]

[a] Institute of Tissue Regeneration Engineering (ITREN), Dankook University, Cheonan, 31116, Republic of Korea
[b] Department of Nanobiomedical Science and BK21 PLUS NBM Global Research Center for Regenerative Medicine, Dankook University, Cheonan, 31116, Republic of Korea
[c] Glass Research Department, National Research Centre, Cairo, 12622, Egypt
[d] Division of Biomaterials and Tissue Engineering, UCL Eastman Dental Institute, 256 Grays Inn Road, London, WC1X 8LD, UK
[e] The Discoveries Centre for Regenerative and Precision Medicine, UCL Campus, London, UK
[f] Department of Biomaterials Science, School of Dentistry, Dankook University, Cheonan, 31116, Republic of Korea
[g] UCL Eastman-Korea Dental Medicine Innovation Centre, Dankook University, Cheonan, 31116, Republic of Korea

ARTICLE INFO

Keywords:
Nanotherapeutics
Mesoporous bioglass nanospheres
Copper ion/Growth factor
Antibacterial/angiogenesis
Osteogenesis/odontogenesis

ABSTRACT

Therapeutic options are quite limited in clinics for the successful repair of infected/degenerated tissues. Although the prevalent treatment is the complete removal of the whole infected tissue, this leads to a loss of tissue function and serious complications. Herein the dental pulp infection, as one of the most common dental problems, was selected as a clinically relevant case to regenerate using a multifunctional nanotherapeutic approach. For this, a mesoporous bioactive glass nano-delivery system incorporating silicate, calcium, and copper as well as loading epidermal growth factor (EGF) was designed to provide antibacterial/pro-angiogenic and osteo/odontogenic multiple therapeutic effects. Amine-functionalized Cu-doped bioactive glass nanospheres (Cu-BGn) were prepared to be 50–60 nm in size, mesoporous, positive-charged and bone-bioactive. The Cu-BGn could release bioactive ions (copper, calcium and silicate ions) with therapeutically-effective doses. The Cu-BGn treatment to human umbilical vein endothelial cells (HUVEC) led to significant enhancement of the migration, tubule formation and expression of angiogenic gene (e.g. vascular endothelial growth factor, VEGF). Furthermore, the EGF-loaded Cu-BGn (EGF@Cu-BGn) showed pro-angiogenic effects with antibacterial activity against *E. faecalis*, a pathogen commonly involved in the pulp infection. Of note, under the co-culture condition of HUVEC with *E. faecalis*, the secretion of VEGF was up-regulated. In addition, the osteo/odontogenic stimulation of the EGF@Cu-BGn was evidenced with human dental pulp stem cells. The local administration of the EGF@Cu-BGn in a rat molar tooth defect infected with *E. faecalis* revealed significant in vivo regenerative capacity, highlighting the nanotherapeutic uses of the multifunctional nanoparticles for regenerating infected/damaged hard tissues.

1. Introduction

Tissues are occasionally infected by bacterial strains from their surrounding environment [1]. Infection is very hostile to repair and regenerate tissues due to the presence of bacteria which interferes with the regeneration process and even adversely affects the surrounding normal tissues [2]. Limited therapeutic options are available for the regeneration of infected dysfunctional tissues. The current clinical therapies for infected tissues are mainly focused on the antibiotics administration. However, due to the limitation of antibiotic therapy, such

Peer review under responsibility of KeAi Communications Co., Ltd.
* Corresponding author. Institute of Tissue Regeneration Engineering (ITREN), Dankook University, Cheonan, 31116, Republic of Korea.
** Corresponding author. Institute of Tissue Regeneration Engineering (ITREN), Dankook University, Cheonan, 31116, Republic of Korea.
*** Corresponding author. Institute of Tissue Regeneration Engineering (ITREN), Dankook University, Cheonan, 31116, Republic of Korea.
E-mail addresses: a.elfiqi@dankook.ac.kr (A. El-Fiqi), ducious@dankook.ac.kr (J.-H. Lee), kimhw@dku.edu (H.-W. Kim).
[1] These authors contributed equally to this work as Co-first author.

https://doi.org/10.1016/j.bioactmat.2020.07.010
Received 2 July 2020; Received in revised form 20 July 2020; Accepted 20 July 2020

as bacterial resistance and adverse side effects (e.g., systemic toxicity), excision of the lesion is inevitably involved which results in loss of tissue and its function [3]. Hence, there is a growing clinical need for developing new and effective therapeutic approaches that can treat tissue infection and restore its regeneration capacity while preserving surrounding healthy tissues and their functionality [4].

Infection of dental pulp has been considered as one of the most common dental diseases; recent report indicates that more than 90% of adults have been exposed to dental pulp infection related diseases [5], underscoring the necessity for developing effective therapeutic approach. Dental pulp tissue is the core non-mineralized soft component of tooth that is full of nerves and blood vessels imparting the tooth its viability [6–10]. Due to the limited capacity of the infected tissue to regenerate under inflamed conditions, removal of infected pulp tissue is widely performed in clinics as a standard procedure. However, this clinical process generally removes the entire pulp tissues including healthy parts to minimize recurrent infection, thus leading to reduced tooth sensitivity and increased tooth fracture [11,12].

Bioactive glass, as a unique class of bioactive materials, has demonstrated remarkable properties for both hard and soft tissue repair and regeneration [13,14]. Bioactive glass offers several merits such as hydroxyapatite (bone-like mineral) formation, biodegradability, and supply of therapeutic bioactive ions (e.g., silicate and calcium that can act as angiogenic and/or osteogenic/odontogenic stimulator). Furthermore, some kinds of ions e.g. Cu, Zn, Sr or Co can be doped to the bioactive glass that is effective for specific therapeutic purposes [15]. Of note, beyond the conventional melt-derived glass processing tool, the sol-gel synthesis of nanoparticle formulations was recently advanced to prepare bioactive glasses into mesoporous nanoparticle forms which significantly altered the physicochemical properties (in terms of morphology, size, textural properties and surface chemistry) and the related biological performance [16,17]. Adding to this, the mesoporous nanoparticle form of bioactive glass has the capacity to intracellular deliver therapeutic molecules (drugs, growth factors, or genes) [16]. Some of the recent studies have reported that mesoporous bioactive glass nanomaterials and their composites/hybrids could demonstrate the capacity for delivering drugs and genes, as well as releasing bioactive ions [18–30].

Here we propose the development of bioactive glass nanoparticles that can effectively regenerate infected tissues of dental pulp. To this end, we focus on several key biological events that are necessary for the effective regeneration of infected pulp tissue, such as antibacterial activity, pro-angiogenesis, and odontogenesis stimulation. In particular, angiogenesis is an indispensable process for tissue regeneration due to that the newly regenerated tissues may encounter limited diffusion of nutrients and oxygen. Our interests here are the copper ions (Cu^{2+}) and epidermal growth factor (EGF) for the synergistic pro-angiogenic effects. In fact, the Cu^{2+} ions are known to possess antibacterial activity [31] as well as pro-angiogenic efficacy [32,33]. The angiogenesis is known through the stimulation of hypoxia-inducible factor (HIF)-1α that is one of the upstream signalling molecules of the vascular endothelial growth factor (VEGF) [34–43]. EGF is an angiogenesis activator that binds its specific receptor, EGFR, expressed on epithelial cells, and it not only stimulates division, growth, and differentiation of endothelial cells but also increases tubule formation and cell migration [44–46]. Therefore, the use of Cu ion together with EGF is consider to reap up the dual therapeutic effects (antibacterial and pro-angiogenic). The release of calcium ions from bioactive glass nanoparticles may help differentiation and mineralization of stem cells in dental pulp, as demonstrated previously [47].

The bioactive nano-delivery system ('nanotherapeutics') proposed here is thus for multiple therapeutic purposes for treating dental pulp tissue; fighting against bacteria with simultaneous boosting of vascularized tissue regeneration. The antibacterial, angiogenesis and odontogenesis properties of the developed nanotherapeutics were characterized in the in vitro cell/bacteria cultures, and the therapeutic efficacy was proved in the infected dysfunctional pulp tissue model in rats. Thus, we have fully demonstrated the efficacy of the nanotherapeutics in a series of in vitro cell studies and in the in vivo tissue model. Collectively, the novelty of this work was demonstrated in terms of significant findings that can be merited in the context of the design and development of novel multifunctional bioactive nanotherapeutics for the regeneration of infected hard tissue defects.

2. Experimental

2.1. Materials

Tetraethoxysilane (TEOS, ≥ 99%), calcium nitrate tetrahydrate (Ca-NTH, ≥ 99%), copper (II) nitrate trihydrate (Cu-NTH, ≥ 99%), polyethylene glycol (PEG, Mn = 10000), ammonium hydroxide, ethanol anhydrous, 3-(Triethoxysilyl)propylamine (APS, ≥ 98%), toluene anhydrous, Tris HCl buffer, 1 N hydrochloric acid, phosphate-based solution (PBS), chemicals for simulated body fluid (SBF), and all chemicals unless otherwise stated were all provided from Sigma-Aldrich. Ultrapure distilled H_2O was utilized wherever needed in experiments.

2.2. Synthesis of nanoparticles

Amine (-NH_2) surface functionalized Cu-doped (Cu-BGn) and Cu free (BGn) mesoporous bioactive glass nanospheres with 85% SiO_2 – 10% CaO – 5% CuO and 85% SiO_2 – 15% CaO (wt%) respectively, were produced by alkali-mediated ultrasonic-coupled sol-gel synthesis. PEG (5 g), Ca-NTH (189 mg for Cu free or 126 mg for Cu-doped) and Cu-NTH (46 mg) were dissolved in 0.15 L of alkaline methanol (pH ~ 12.5). TEOS (884 mg in 0.03 L methanol) was then added while stirring vigorously with ultrasound application (20 min, 10 s on/off mode). The formed precipitates were collected and cleaned with dH_2O/alcohol for 3 times via vortexing (1000 rpm)/centrifuging (5000 rpm). The collected precipitates were kept in drying oven for 12 h and then calcined under airflow (600 °C, 5 h). Finally, the produced nanopowders of BGn and Cu-BGn were dispersed at 2 mg/mL in 2% (v/v) APS-Toluene mixtures and then refluxed (80 °C, 24 h). The powders were then separated, washed thrice with toluene and finally dried (80 °C, 12 h). The prepared nanopowders were stored in vacuumed sample box.

2.3. Characterizations of nanoparticles

The amorphous structures of amine (-NH_2) surface functionalized BGn and Cu-BGn were confirmed by X-ray diffraction (XRD, Rigaku-Ultima IV). The chemical composition of Cu-BGn was ensured from SEM-EDS analysis (Quantax, Bruker). The nanoparticle morphology, microstructure, and particle size were investigated with transmission-electron microscope (TEM, JEOL). The average particle diameter was estimated via diameter measurements of nanospheres (n = 100) in TEM images using particle size analysis software. Textural properties were determined by N_2-sorption analysis (Quadrasorb SI). The surface area was obtained by BET equation while porosity parameters were determined using NLDFT method. The surface charge was determined with a ζ-potential measurement (Zetasizer Nano ZS). The ζ-potential was measured in dH_2O (pH 7.4, 25 °C) and it was obtained from five different measurements. The phase and characteristic structural groups before and after SBF immersion were examined by XRD and Fourier-transform infra-red instrument equipped with ATR accessory unit (ATR-FTIR, Varian 640-IR).

The release of SiO_4^{4-}, Ca^{2+}, and Cu^{2+} bioactive ions from amine (-NH_2) surface functionalized BGn and Cu-BGn nanospheres were detected by ICP-AES. Nanopowder (50 mg) was soaked in 10 mL Tris/HCl buffer (pH 7.4, 37 °C) and kept under 120 rpm continuous shaking. The release media were collected at pre-determined time intervals and then

separated (15,000 rpm, 10 min). The collected solutions were analyzed with ICP-AES (Optima 4300DV). Three replicate samples were examined (Average ± S.D.)

2.4. In vitro cytotoxicity

3200 cells/100 μL of primarily cultured human multipotent stem cells in dental pulp (hMSCs) and human endothelial cells (HUVEC, ATCC PCS-100-010) were plated onto each well of 96-well plates for 1 day. Then, the various concentrations of nanospheres were treated for further 24 h. The primary culture was made using extracted cells from a human third molar tooth. For hMSCs, alpha-MEM (LM 008-01, Welgene) was supplemented with fetal bovine serum (10%, Gibco), GlutaMAX (2 mM, Gibco), L-ascorbic acid (0.1 mM, Sigma), and penicillin-streptomycin (1%, Invitrogen) as a growth medium for proliferating hMSCs. Then, for differentiation assay, β-glycerophosphate (10 mM), ascorbic acid (50 μg/mL), and dexamethasone (100 nM) was further added to the normal growth medium for making an osteo/odontogenic medium (OM). For HUVEC, vascular cell basal medium (ATCC PCS-100-030) containing endothelial cell growth kit-VEGF (ATCC PCS-100-041) with 1% penicillin-streptomycin (Invitrogen) was used. The viability of cells (n = 6) was assessed by a water-soluble tetrazolium salt assay (EA-Cytox, Daeil Lab, Korea). The absorbance (λ = 450 nm) was detected (SpectraMax M2e, Molecular Devices) and normalized to the control group (cell only without nanospheres) to represent cell viability. Live and dead assay were performed with kits (L3224, Thermo Fischer, Waltham, MA) and images were visualized with under a confocal laser microscope (LSM 700, Carl Zeiss). All analyses were performed in triplicate, and the mean ± SD from absorbance and images was displayed.

2.5. In vitro osteo/odontogenesis study

The hMSCs were cultured with various concentrations of BGn or Cu-BGn in each well of 24-well plates for pre-determined time points up to 7 days either with or without OM. For qPCR analysis, total 1 μg RNA extracted using Ribospin (GeneAll, Seoul, Korea) was reverse-transcribed to cDNA using a pre-mixture (AccuPower RT PreMix, Bioneer, Korea) and oligo-dT (Venlo, Netherlands, Qiagen) by a 2720 Thermal Cycler (Applied Biosystems). The quantitative mRNA expression level was measured with SYBR Green (Applied Biosystems) according to the manufacturer's instructions by real-time PCR machine (StepOnePlus, Applied Biosystems). The primer sequences for osteo/odontogenesis described elsewhere [21]; Glyceraldehyde 3-phosphate dehydrogenase (GAPDH), collagen type 1 alpha (COL1 A), dentin sialophosphoprotein (DSPP), dentin matrix protein 1 (DMP1), and osteocalcin (OCN). After checking qPCR efficiency, the mRNA expression levels of each group were calculated as the relative fold change with respect to hMSCs cultured with growth media after being normalized to GAPDH, based on the 2-(delta) (delta) Ct value by StepOne software v2.3 (n = 4). The mean ± SD was shown after independent triplicate experiments.

For cellular mineralization tests, hMSCs were cultured with the nanospheres under OM in 12 well plates for 28 days (n = 5). After the cells were stained with alizarin red S (ARS) solution after fixation with formaldehyde (10%), ARS stained images were visualized using a light microscope. To elute the stains for quantification, each well was immersed with 10% cetylpyridinium chloride in sodium phosphate and the optical density was determined (λ = 562 nm). All experiments were done in triplicate.

2.6. Cell internalization

To picture the cellular internalization of nanospheres into hMSCs and HUVEC, TEM analysis was used. After the cells were treated with nanospheres (10 μg/mL) for 4 h, the cells were fixed, dehydrated and infiltrated with propylene oxide before embedding (Poly/Bed 812, Polysciences, Warrington, PA, USA). After sections (70 nm thickness), double-staining with uranyl acetate and lead citrate was performed and observed by TEM (JEM-1011, JEOL).

To reveal the cellular internalization pathway, sodium azide (100 mM, Sigma), amantadine hydrochloride (1 mM, Sigma), 5-(N-ethyl-N-isopropyl) amiloride (2.5 mM, Sigma) or genistein (100 mM, Sigma) was pretreated to cells for 1 h. Then, 10 μg/mL of FITC-conjugated-nanospheres were added for another 4 h culture. Cells were co-incubated with nanospheres at 4 °C for 4 h to confirm ATP-dependent endocytosis. After being trypsinized, a flow cytometer (FACS Calibur, BD Biosciences, San Jose, CA, USA, 10,000/ea, n = 3) was performed for quantification (CellQuest Pro, v.5.1 BD Biosciences).

2.7. Angiogenesis study

For testing angiogenesis, thick matrigel (356,234, Corning, NY, USA) coating was performed on 24 well plates and HUVECs (2×10^5/mL of 0.5 mL) were seeded on. qPCR analysis was performed after 2, 4, 6, and 12 h of culturing with nanospheres according to the previous methodology. The primers sequence for angiogenesis is provided in supporting information (Table S1). The tubular formation was optically captured after 12 h by microscope (IX-71; Olympus). Random images in each group were selected for the measurement of the tubular formations (n = 3). For migration assay, 1.0×10^5 cells were seeded for 24 h to get confluence. Mitomycin B (10 μg/mL, Sigma) was pre-incubated with cells for 2 h in basal HUVEC media without supplement to minimize proliferation. After scratching using a 200 μL tip, nanospheres were treated and images were visualized up to 24 h by light microscopy (IX-71; Olympus). FGF2 treated group (5 ng/mL) was used as a positive control.

2.8. EGF loading and in vitro release

To optimize the loading efficiency of Cu-BGn, various concentration of epidermal growth factor (EGF, 0–1000 μg/mL) was incubated onto 1 mg of Cu-BGn for 2 h at 37 °C, possibly accelerating angiogenesis via synergistic effects. The release of EGF from Cu-BGn-EGF complex (1.45 mg) loaded with the maximum amount of EGF per mg of Cu-BGn was gathered in 1 mL of PBS (37 °C) at pre-determined time points up to 7 days. For measuring EGF amount, after centrifuge (13,000 g, 5 min), the supernatant was used for determining the amount of EGF and finally calculated by human EGF standard ABTS ELISA development kit (Peprotech, USA).

2.9. VEGF secretion

To determine the efficacy of the EGF@Cu-BGn complex, VEGF secretion in media was calculated using a human VEGF165 standard ABTS ELISA development kit (Peprotech, USA). After seeding HUVECs (3200 cells/100 μL) on 96 well plates and 24 later, supplemented HUVEC medium was newly added with nanospheres. After 12 h, the VEGF amount was measured (n = 3). As control groups for separate growth factor treatment along with nanoparticle, 4.5 μg/mL of free EGF was separately added with 10 μg/mL of Cu-BGn nanospheres. Also, to verify the angiogenic role of copper ions in media, 25 μM of TEPA, chelating free copper, was co-treated. In the case of LPS challenge to HUVEC, LPS (10 μg/mL) was co-treated to cells when nanospheres were treated.

2.10. In vitro antibacterial effects

In vitro antibacterial tests were performed using tooth pulp infection with bacteria, *Enterococcus faecalis* (*E. faecalis*, ATCC 19433). Bacteria (1×10^5/mL) in the log phase were cultured with nanospheres in 12 wells under PrestoBlue (10%, Molecular probes, Invitrogen, Waltham, USA) for up to 5 h. The absorbance (λ = 570 nm–600 nm)

was detected by a microplate reader (Spectra Max M2e) from the incubating solution (100 μL) transferred to 96 well (n = 5) at determined time. Chlorhexidine digluconate (2%, Sigma) was used as a positive control. The assays were performed in triplicate independently and representative data sets were shown.

2.11. Bacteria/HUVEC co-culture

The co-culture experiment of HUVECs and bacteria was further carried out by a modified protocol reported elsewhere [48]. The infection conditions included LPS (10 μg/mL) and *Enterococcus faecalis* (*E. faecalis*, ATCC 19433, 10^4 CFU/mL) which were co-treated to the HUVECs and the effects of nanospheres were investigated. The VEGF secretion was also quantified in the co-culture of bacteria/HUVECs.

2.12. In vivo implantation, histology and immunostaining

For vivo study, the clinically relevant inflamed dental-pulp tissue model was used as reported elsewhere [49,50]. All in vivo studies were performed after approval by the Dankook University Animal Care and Use Committee (license number: 12-027). Briefly, total ten male SD rats (6 weeks old, 150–180 g) were administrated with a mixture of ketamine and xylazine for the anesthetization. Upper first molar tooth (n = 20, each group n = 5) was drilled under water-cooling to produce a round-shaped defect (diameter = 0.8 mm). After the pulp tissue was equally infected by E. faecalis suspension (1×10^5 CFU in 5 μL), nanoparticle paste with DW at 0.5 mg/mL powder-to-liquid was applied to the defect and a light-cure dental resin (CharmFil, Korea) with dental adhesive (All-bond universal, Bisco, Schaumburg, USA) was filled over. All filled teeth occlusal were flattened to minimize biting-force-load on the site of surgery. Animals were randomly assigned into four groups: i) control (sterilized cotton roll), ii) BGn (1.5 mg), iii) Cu-BGn (1.5 mg), iv) EGF loaded Cu-BGn (2.25 mg) treatment (n = 5). At six weeks' post-operation, all fillings were manually confirmed to have no failure of restorations. After hard tissue formation was examined by μ-CT, histological features were observed by H&E staining.

For the immunohistochemistry, the tissue samples were incubated with primary antibody including angiogenesis marker CD31 (H-3; PECAM-1. Santa Cruz, SC-376764) and macrophages activation marker iNOS (M1 macrophage marker, Abcam, ab15323) at 4 °C overnight. The samples were then treated with secondary antibody (FITC or Rhodamine) for 1 h and counterstained with DAPI for 5 min at room temperature. Images were observed under a confocal laser microscope (Zeiss LSM 700, Germany) and quantified using Image J software (n = 5).

2.13. Statistics

Data are shown as mean ± standard deviation (SD) after at least three independent experiments. One-way ANOVA with Tukey's post hoc test was performed to compare groups, and p-value < 0.05 was considered significant.

3. Results and discussion

3.1. Characteristics of nanoparticles

3.1.1. Morphology and physicochemical properties

TEM imaging of amine (-NH_2) surface functionalized BGn and Cu-BGn (Fig. 1 a and b) unveiled spherical mesoporous nanospheres with diameters of 64.2 ± 4.1 nm and 52.4 ± 5.3 nm, respectively. It is evident that CuO (a silica network modifier) added in replacement of CaO in BGn exerted some influence on the particle size. This might be explained in terms of differences in ionic radii of Ca^{2+} and Cu^{2+} ions as Cu^{2+} ion has a smaller ionic radius (0.73 Å) compared to that of Ca^{2+} (0.99 Å) [51]. Representative EDS spectrum (inset of Fig. 1b) ensured the presence of Si, Ca, and Cu in the chemical composition of Cu-BGn with weight % ratio of Si: Ca: Cu = 85.4: 9.7: 4.9. Optical photos of as-prepared BGn and Cu-BGn nanopowders (inset in Fig. 1 c) show that BGn possess white colour while Cu-BGn has a blue-green colour which originates from d-d transitions involving Cu^{2+} (d^9) ions [52]. The XRD (Fig. 1 c) confirmed the amorphous structure of BGn and Cu-BGn as evidenced from the complete absence of XRD diffraction peaks and the presence of a broad halo (at 2 Θ = 20° to 30°) characteristic of amorphous materials [53]. Representative XPS wide survey spectrum (Fig. 1 d) of the amine surface functionalized Cu-BGn detected signals of Si 2p (103.17 eV), Si 2s (153.81 eV), C1s (284.86 eV), Ca 2p (347.57 eV), N1s (399.66 eV), Ca 2s (439.2 eV), O1s (532.27 eV) and Cu 2p (933.2 and 953.72 eV) [54]. Furthermore, high resolution XPS deconvoluted spectra of Cu $2p_{2/3}$ is shown in inset of Fig. 1 d in addition to Si 2p, Ca 2p, O1s, N1s, and C1s shown in Fig. S1 (a-f). The deconvoluted XPS spectrum of Cu 2p (inset of Fig. 1 d) revealed two signals at 933.2 eV and 935.65 eV, assigned to Cu $2p_{3/2}$ core levels of Cu^{2+} ions [41,55]. The XPS analysis revealed the atomic bonding status and structural atomic environments of the Si, Ca, O, Cu, C and N and confirmed the electronic state of Cu^{2+} in the glass matrix of Cu-BGn.

Fig. 1 (e) and the inset show the N_2-isotherms and pore size distributions of amine surface functionalized BGn and Cu-BGn. The N_2-isotherms belong to Type-IV isotherm with H_4 hysteresis loop which is exhibited by mesoporous materials [56]. The pore size distribution (inset of Fig. 1 e) showed that BGn possess pores with 3.8, 4.1, 6.1, 8.1 and 10.5 nm in size whereas, Cu-BGn possess pores with 3.5, 4.1, 5, 7, 8.1 and 12.1 nm in size. The average pore size and total pore volume were estimated for BGn as 7.7 ± 0.01 nm and 0.084 ± 0.004 cm^3/g, respectively. Whereas for Cu-BGn, those values were calculated as 8.8 ± 0.06 nm and 0.087 ± 0.006 cm^3/g, respectively. The BET specific surface areas of BGn and Cu-BGn (Table S1) were determined as 37.9 ± 1.8 and 44.9 ± 3.2 m^2/g, respectively. The BGn and Cu-BGn have positively charged surfaces with zeta potentials of +20.2 ± 0.71 mV and +25.3 ± 0.36 mV in magnitude, respectively. The positive charges of BGn and Cu-BGn are due to the presence of surface amine (-NH_2) groups introduced by APS functionalization as confirmed by ATR-FTIR spectra shown in Fig. S2 (a) which identified IR bands associated with amine groups as labelled on the spectra. The surface areas, textural properties and zeta potentials of amine surface functionalized BGn and Cu-BGn are summarized in Table S1.

3.1.2. In vitro release of bioactive ions

The release profiles of SiO_4^{4-}, Ca^{2+}, and Cu^{2+} ions from amine surface functionalized Cu-BGn and BGn are depicted in Fig. 1 (b) and Fig. S2 (b), respectively. A quick linear release of SiO_4^{4-}, Ca^{2+}, and Cu^{2+} ions has been observed within the first 24 h of immersion. In this early period, BGn released about 440 ppm of Ca^{2+} ions and 365 ppm of SiO_4^{4-} ions, while Cu-BGn released about 167 ppm of Ca^{2+} ions, 308 ppm of SiO_4^{4-} ions and 79 ppm of Cu^{2+} ions. In the next period, the release of Ca^{2+} and Cu^{2+} ions started to slow down with gradual release and then reached a plateau after 72 h of release. Whereas, SiO_4^{4-} ions release from BGn and Cu-BGn showed increased and continual release up to 168 h (7days) of release. The release of Ca^{2+} and SiO_4^{4-} ions from BGn reached about 496 ppm and 603 ppm respectively, after 168 h of release. Whereas, the release of Ca^{2+}, SiO_4^{4-}, and Cu^{2+} ions from Cu-BGn reached about 296 ppm, 559 ppm, and 152 ppm respectively, after 168 h of release. Of note, the release of SiO_4^{4-} ions from BGn and Cu-BGn showed almost similar release profiles with remarkable released amounts of SiO_4^{4-} ions attributed to the dissolution of BGn and Cu-BGn matrices in addition to dissolution of their APS surface groups [29]. The release of Ca^{2+} ions from BGn and Cu-BGn showed very similar release profiles. However, Cu-BGn released fewer amounts of Ca^{2+} ions due to the partial replacement of 5 wt% of CaO with 5 wt% of CuO in the chemical composition of BGn (85% SiO_2 – 15% CaO). Finally, the release of Cu^{2+} ions showed initial linear release up to 24 h then slowed-down with constant gradual

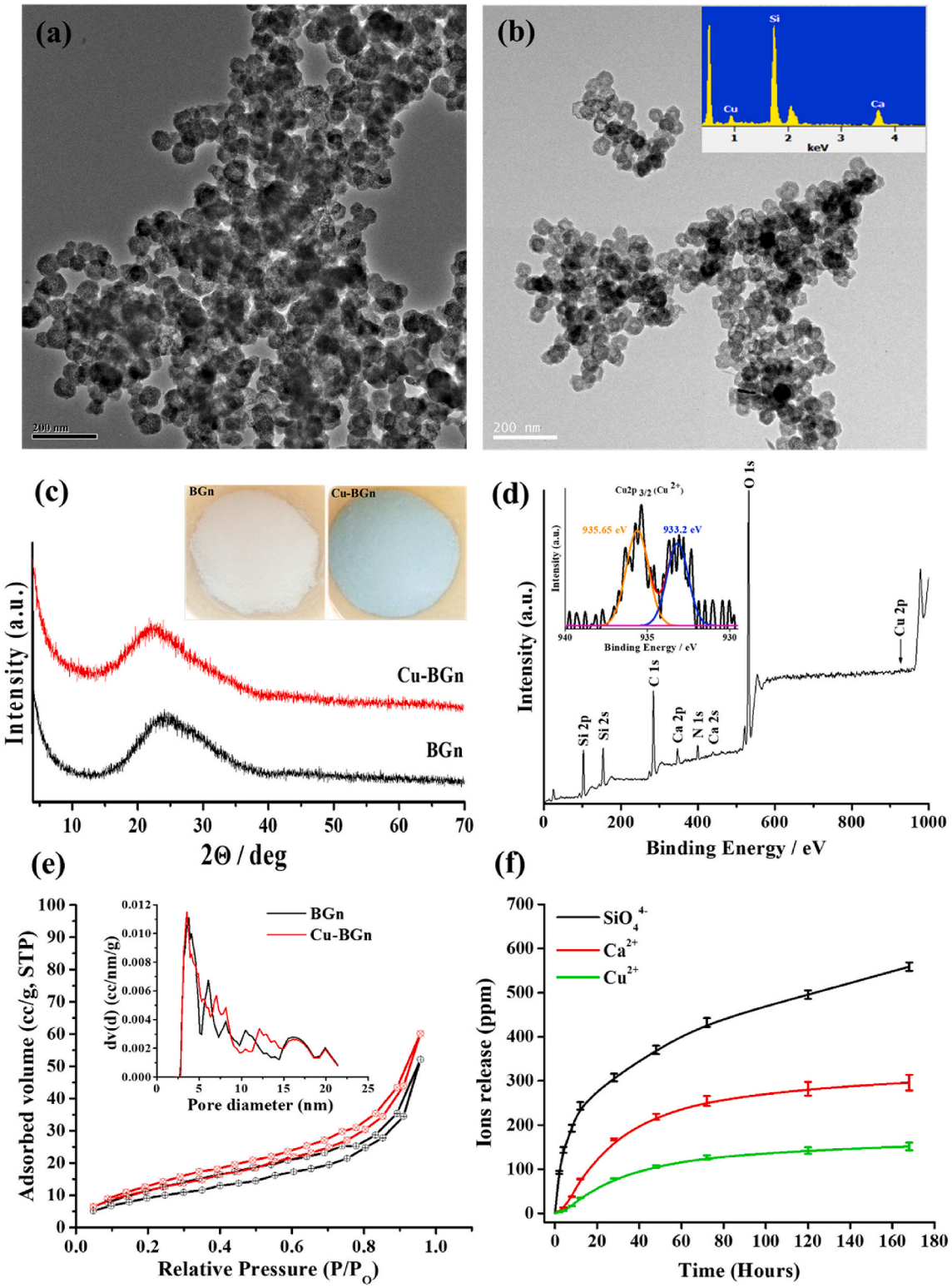

Fig. 1. Characteristics of amine (-NH_2) surface functionalized BGn and Cu-BGn: TEM images of BGn (a), Cu-BGn (b) and representative EDS spectrum of Cu-BGn (inset in b). XRD spectra (c) and optical photos of as-prepared BGn and Cu-BGn. (inset in c). Representative wide survey XPS spectrum of amine (-NH_2) surface functionalized Cu-BGn showing peaks of Si 2p, Si 2s, C1s, Ca 2p, Ca 2s, N1s, O1s and Cu 2p core levels (d). High resolution deconvoluted XPS spectra of $Cu2p_{3/2}$ core level is shown in inset of (d). N_2-sorption isotherms with pore size distribution (e and inset in e) showing existence of various pore sizes in the nanospheres. Release profiles of SiO_4^{4-}, Ca^{2+} and Cu^{2+} bioactive ions from amine (-NH) surface functionalized Cu-BGn during immersion in physiological-like conditions at 37 °C and pH 7.4 as determined by ICP-AES (f). Cu-BGn showed excellent release of SiO_4^{4-}, Ca^{2+} and Cu^{2+} bioactive ions with therapeutically effective-doses.

release up to 7days. Taken together, the ions release profiles showed the ability of Cu-BGn to release therapeutic ions with biologically relevant doses to effectively stimulate cellular processes such as osteogenesis and angiogenesis [32–38]. Furthermore, the released concentrations of Cu^{2+} ions are highly capable to exert antibacterial actions [31,36].

3.1.3. Acellular in vitro apatite forming ability

The in vitro hydroxyapatite forming property of Cu-BGn was evaluated by XRD and FT-IR examinations of SBF-immersed Cu-BGn (Fig. S2 c-d). The hydroxyapatite formation was detected after 3 days of SBF immersion as noticed from a weak peak in the XRD spectra shown in Fig. S2 (c). The hydroxyapatite formation then increased remarkably after 7, 14 and 21 days of SBF immersion as witnessed from the increased intensities of the XRD diffraction peaks. All the evolved XRD diffraction peaks belong to the hydroxyapatite phase, namely reflections from 002, 211, 300, 130, 222, 213, and 004 as indexed on the XRD spectra and according to JCPDS card No. 09-0432 [29,57]. The initial delay in hydroxyapatite formation of Cu-BGn is probably owing to the leach out of Cu^{2+} ions to the surrounding medium which initially overlap and retard the formation and nucleation rate of amorphous calcium phosphate and its crystallization into hydroxyapatite [58]. The FT-IR spectra of SBF-immersed Cu-BGn (Fig. S2 d) further confirmed the trend of hydroxyapatite formation rate and it came in a very good agreement with XRD spectra. The IR spectrum contained phosphate functional groups with frequencies at 562 cm^{-1}, 601 cm^{-1}, and 1028 cm^{-1}. The band at 1061 cm^{-1} is ascertained to silicate groups of Cu-BGn while the phosphate band at 1028 cm^{-1} (inset graph) is evolved with increasing SBF immersion time [29,59]. The spectra also showed bands at 872 cm^{-1}, 1417 cm^{-1}, and 1451 cm^{-1}, assigned to carbonate groups (CO_3^{2-}) [59]. Collectively, XRD and FT-IR have clearly demonstrated the in vitro hydroxyapatite-formation ability of amine surface functionalized Cu-BGn.

3.2. HUVECs viability and nanospheres internalization pathways

The cell viability and nanoparticle internalization were examined on HUVECs (Fig. 2). HUVECs were cultured with various doses (0, 2.5, 5, 10, 20, 40, and 80 μg/mL) of BGn and Cu-BGn and their viability was determined. The live (green)/dead (red) staining is shown in Fig. 2 (b). The HUVECs viability gradually decreased over nanoparticle concentration up to 40 μg/mL down to 30% (for BGn). Whereas, it increased to 107% at 10 μg/mL and then gradually decreased to 10% at 80 μg/mL (for Cu-BGn). Interestingly, Cu-BGn showed higher cell viability in the concentration range (10–20 μg/mL) than BGn ($P < 0.05$), probably due to the combined effects of differently released Ca and Cu ions; the ICP data for 7 days hint lower Ca ions release from Cu-BGn than from BGn (440 ppm vs. 167 ppm for 7 days) while Cu ions release was only from Cu-BGn (152 ppm for 7 days) although the exact mechanism of the combined effects on cell viability needs further investigation [60,61]. The live/dead cell stained images confirmed the same trend obtained from cell viability assay. Intercellular mechanism by nanospheres was performed after 4 h treatment at 10 μg/mL. The internalized nanospheres were tracked and visualized by TEM as displayed in Fig. 2(c–d). The nanospheres uptake efficiency was quantified by flow cytometry ($n = 3$) using rhodamine-conjugated nanospheres. Furthermore, to elucidate the endocytosis mechanism, pretreatments of HUVECs cells (for 1 h) with sodium azide (SA), amiloride (AL), amantadine-HCl (AT) or genistein (GE) were performed as an inhibitor of ATP-dependent, macropinocytosis, caveolae-mediated, or clathrin-mediated endocytosis respectively. HUVECs cells were also incubated at 4 °C to prevent ATP-dependent endocytosis then after 4 h of treatment, rhodamine positive cells were counted by flow cytometry as shown in Fig. 2 (e).

Nanospheres internalize into cells through various pathways e.g. ATP-dependent endocytosis including membrane structural changes or nonspecific diffusion [21]. The uptake of nanospheres significantly decreased in SA treatment along with ATP-depletion culture condition (4 °C) as shown in Fig. 2 (e), confirming ATP-dependent endocytosis. Furthermore, the ATP-dependent endocytosis can happen in non-immune cells through either macropinocytosis or receptor (i.e. clathrin or caveolae)-mediated endocytosis [21]. For screening out which pathway would be involved, we used the above-stated pre-treatment conditions to block specific endocytosis. It was found that the pre-treatment with amiloride (2.5 mM), an inhibitor of micropinocytosis, decreased the uptake efficiency down to 50% indicating that macropinocytosis is the most probable pathway for the nanoparticle internalization.

3.3. In vitro osteogenesis/odontogenesis of hMSCs

After investigating the ATP-dependent macropinocytosis into endothelial cells, the internalization pathway of nanospheres was again evaluated with hMSCs. Internalized Cu-BGn in hMSCs were visualized by TEM (red asterisks), displaying the intracellular position of Cu-BGn in endosomes (Fig. S3 a). The uptake of Cu-BGn significantly ($P < 0.05$) decreased as shown in Fig. S3 (b), confirming that the cellular uptake of Cu-BGn was through ATP-dependent endocytosis (under conditions of 4-degree cell culture and sodium azide, an inhibitor of ATP-dependent endocytosis, treatment) and micropinocytosis in part, similar to HUVECs. we next differentiated hMSCs into osteogenic/odontoblastic cells. The hMSCs were cultured in a differentiation media containing 2.5, 5, or 10 μg/mL of BGn or Cu-BGn respectively and their osteogenic/odontogenic maturation was investigated. The cellular mineralization at 28 days by ARS staining Fig. S3 (c) revealed enhanced red-colored mineralized nodules in Cu-BGn and BGn compared to control (OM, Fig. S4b). Of note, there was a gradual increase in cellular mineralization associated with Cu-BGn in a concentration-dependent manner. Moreover, the osteogenic/odontogenic genes (COL1A, DMP-1, DSPP, and OCN) were significantly improved as shown in Fig. S3 (d), up to 7 days for both nanospheres in comparison to control ($P < 0.05$). Specifically, the early osteo/odontogenic gene marker (COL1A) was upregulated on day 1, while the late osteo/odontogenic gene markers (DMP-1, DSPP, and OCN) were highly expressed on day 3 and 7 [62–65]. Taken together, Cu-BGn had similar differentiation potential compared to BGn and their cellular internalization was partially mediated by ATP-dependent micropinocytosis.

3.4. In vitro angiogenesis of HUVECs

To investigate in vitro angiogenesis associated with BGn and Cu-BGn, the tubular formation of HUVECs on a Matrigel soft matrix was examined for 12 h. Representative images (Fig. 3 a) were taken after 12 h showing the tubular formation of HUVECs induced by BGn and Cu-BGn. Furthermore, the quantification of HUVECs tubular formation in terms of the number of branching points and tube length and was executed as depicted in Fig. 3 (b) and Fig. S4(a), respectively. Another key behaviour associated with angiogenesis is the recruitment of endothelial cells to the site of interest for forming tubules. Migration of HUVECs was investigated for 24 h under 2 h of mitomycin C pretreatment to inhibit cell doubling (Fig. S4 b). Migration of HUVECS was gradually enhanced in the case of Cu-BGn over concentrations of 2.5–10 μg/mL ($P < 0.05$) while BGn displayed a similar migration rate compared to the control ($P > 0.05$). FGF2 (5 ng/mL) treatment was used for positive control, indicating almost double of migration rate. Furthermore, angiogenic gene expression levels including VEGF, VEGFR, bFGF, bFGFR, and eNOS under Cu-BGn in various doses (2.5, 5, and 10 μg/mL) versus BGn (10 μg/mL) were identified by *q*RT-PCR after 2 h, 4 h, 6 h, and 12 h as shown in Fig. 3(d-g). After 2 h and 4 h, eNOS was significantly expressed and showed increased expression with increasing Cu-BGn concentration (Fig. 3 d-e). Also, bFGF showed significant expression only at 10 μg/mL of Cu-BGn. After 6 h, eNOS, bFGFR, VEGF and VEGFR were significantly expressed and showed increased expression with increasing Cu-BGn concentration (Fig. 3 e). After 12 h, eNOS, bFGF, bFGFR, VEGF and VEGFR were significantly expressed and showed increased expression with increasing Cu-BGn concentration (Fig. 3 g). The VEGF promotes angiogenesis by stimulating endothelial cells to develop new blood vessels [66]. Also, bFGF and eNOS stimulate angiogenesis by its potent mitogenic activity for endothelial cells of vicinity [67,68]. Accordingly, these gene expression

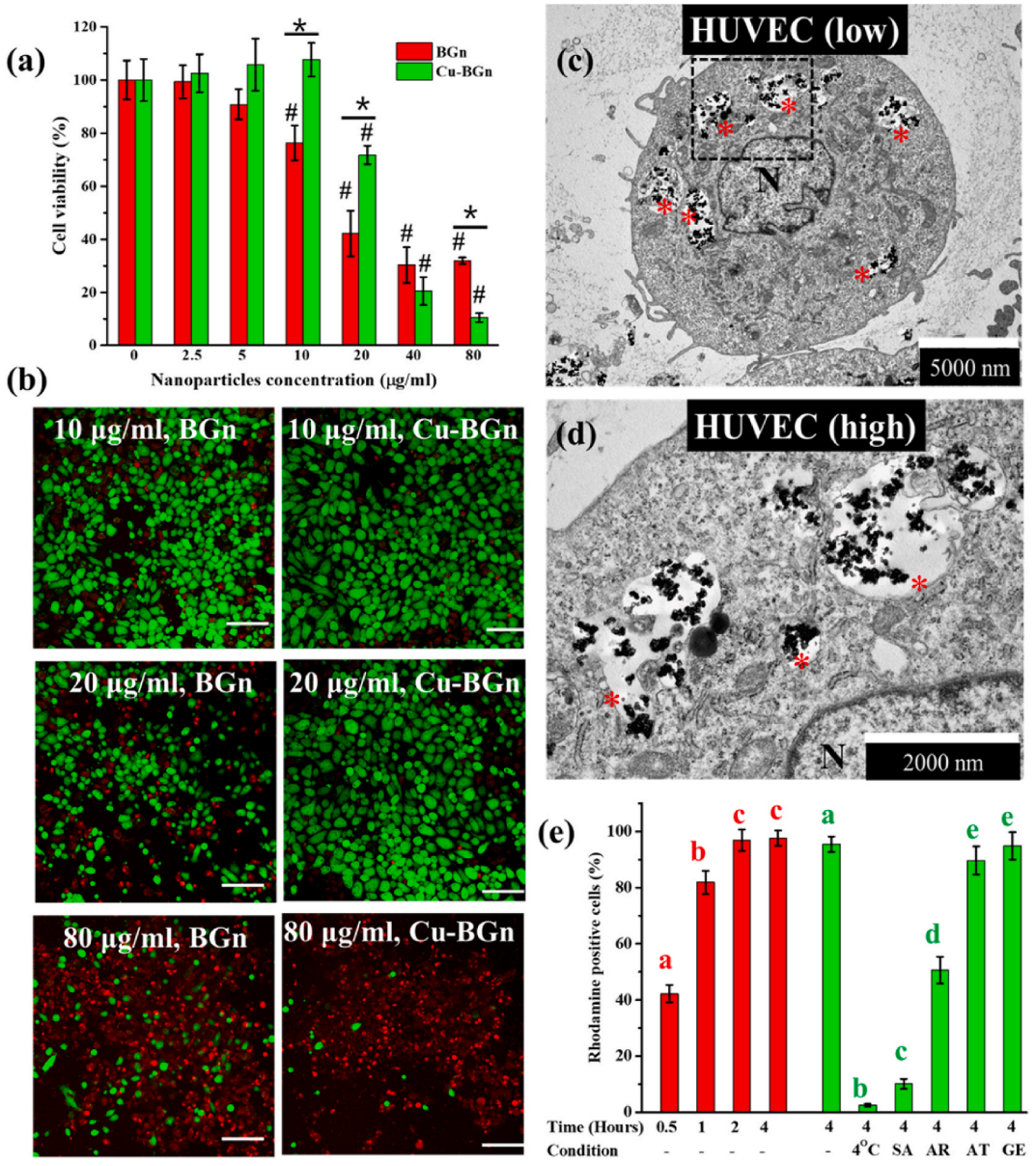

Fig. 2. Cell viability and internalization of nanospheres into HUVECs. Cell viability under different concentrations (0, 2.5, 5, 10, 20, 40, and 80 μg/mL) of BGn and Cu-BGn, (a–b) as measured by water-soluble tetrazolium salt assay and live (green)/dead (red) staining (*compared to no-treatment control, n = 6, $p < 0.05$ and # comparison between BGn and Cu-BGn at $p < 0.05$). Scale bar: 200 μm. Nanoparticle (10 μg/mL) internalization to HUVEC cells after 4 h treatment. Internalized nanospheres were visualized by TEM (c–d); red asterisks (the intracellularly uptaken nanospheres in endosomes) and N (nucleus). Quantitative analysis of intracellularly uptaken nanospheres (e) by flow cytometry (n = 3) after rhodamine-conjugation; depending on the NPs incubation time up to 4 h and chemical-pretreatment conditions, rhodamine positive cells were counted. To reveal endocytosis mechanism, cells were pretreated (1 h) with several chemicals; sodium azide (SA, inhibitor of ATP-dependent endocytosis), amiloride (AL, inhibitor of macropinocytosis), genistein (GE, inhibitor of caveolae-mediated endocytosis), or amantadine-HCl (AT, inhibitor of clathrin-mediated endocytosis) according to the previous protocol [26]; 4 °C incubation used to prevent ATP-dependent endocytosis. Nanospheres significantly decreased in SA treatment along with ATP-depletion culture condition (4 °C), confirming ATP-dependent endocytosis. Furthermore, it was found that the pre-treatment with amiloride (2.5 mM), an inhibitor of micropinocytosis, decreased the uptake efficiency down to 50% indicating that macropinocytosis is the most probable pathway for the nanoparticle internalization. Letters (a, b, c, d and e) indicate significant differences among the groups at $p < 0.05$.

profiles indicate pro-angiogenic capacity of Cu-BGn compared to BGn. Taken together, Cu-BGn enhanced transcription level of key angiogenic gene regulators including eNOS, bFDFR, bFGF, VEGFR and VEGF to about 3–10 times more than BGn. It also improved endothelial cell behaviors such as tubular formation (20–30%) and migration (~40%) compared to BGn and negative control cases. Although silicate ions are known to enhance angiogenesis [42], it seems that the released silicate ions when using a 10 μg/mL of Cu-BGn couldn't match the effective silicate concentration for enhancing angiogenesis [42,66] whereas, the concentration of released Cu^{2+} ions was sufficiently above the minimum concentration required for inducing therapeutic angiogenesis (~0.1 ppm daily) [60,69–72].

3.5. EGF delivery for enhancing VEGF secretion

To further potentiate the angiogenic effect of Cu-BGn, EGF as a negatively charged pro-angiogenic growth factor [73] was loaded into pores of amine surface functionalized Cu-BGn and its loading and release profiles were investigated as shown in Fig. 4. Approximately 33 wt% of EGF (0.45 mg of EGF/total of 1.45 mg of EGF@Cu-BGn) was

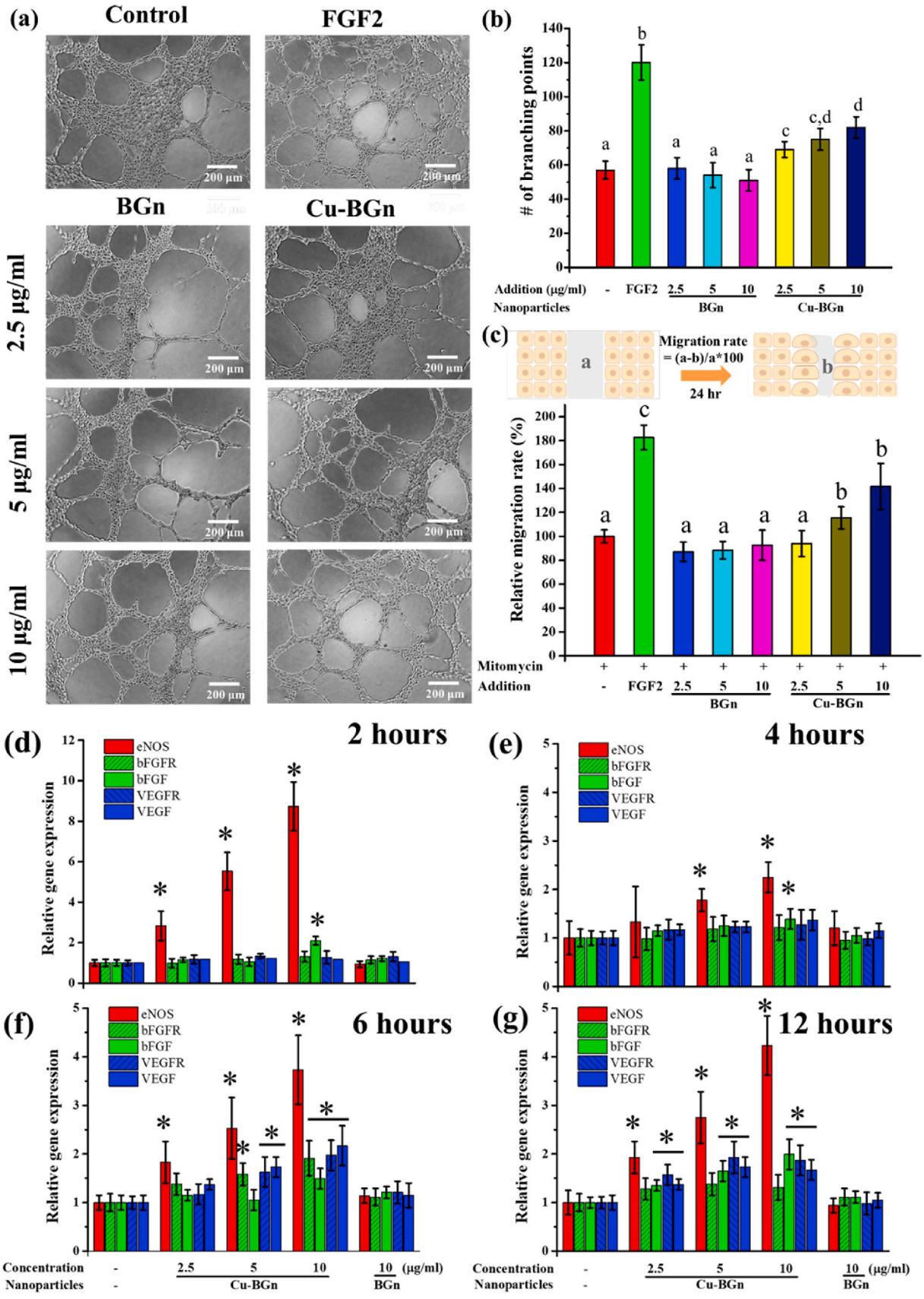

(caption on next page)

Fig. 3. Enhanced tubule formation of HUVEC with Cu-BGn: Representative images (a) after 12 h (n = 3). FGF2 (5 ng/mL) treatment was used as a positive control. Quantification data of HUVEC tubular formation in terms number of branching points (b), revealing increase of tubular formation with Cu-BGn in a dose dependent manner compared to negative control and BGn counterpart. Enhanced migration of HUVEC by Cu-BGn as quantified in (c). Letters (a, b, c and d) indicate significant differences among the groups at $p < 0.05$. Effects of the Cu-BGn treatment on angiogenesis of HUVECs. Angiogenic gene expressions (eNOS, bFGFR, bGFG, VEGFR, VEGF) at 2, 4, 6, and 12 h (d–g). The treatment groups are the same through (d–g). Upregulation of angiogenic genes were detected with Cu-BGn in a dose dependent manner compared to untreated control and BGn counterpart. (* comparison between BGn and Cu-BGn, $p < 0.05$, n = 4).

loaded into 1 mg of Cu-BGn (Fig. 4 a). EGF rapidly released 60% of the total loaded amount from EGF@Cu-BGn during the first 24 h and then released in a relatively slow pattern for the next 6 days at a rate of 26.6 μg/day (Fig. 4c), which is considered an effective concentration for promoting pro-angiogenesis [69]. To investigate a possible synergistic effect of released EGF and Cu ions, VEGF secretion from HUVECs was quantified by ELISA in FBS and growth factor reduced media (Fig. 4d). As expected, concentration-dependent increases of VEGF secretion were detected in Cu-BGn treated groups. Strikingly, a synergistic increase of VEGF production was observed in 14.5 μg/mL of EGF@Cu-BGn compared to each component counterpart (10 μg/mL of Cu-BGn and 4.5 μg/mL of EGF). However, separation treatment of Cu-BGn (10 μg/mL) and EGF (4.5 μg/mL) revealed similar VEGF secretion compared to EGF@Cu-BGn (14.5 μg/mL), possibly due to limitation of static culture condition. To reveal the effect of Cu^{2+} ions on enhancing VEGF secretion, TEPA, specific chelator of Cu ions, was co-cultured with Cu-BGn with or without EGF, showing elimination or decrease of VEGF production. Also, this supports the crucial pro-angiogenic role of Cu ions within this system [42].

3.6. In vitro antibacterial effects

Cu^{2+} ions are considered to have not only angiogenic capacity but also antibacterial activity in vitro. The antibacterial effects of nanospheres were initially studied against *E. faecalis*, which is known to be one of the most frequently found pathogens of the pulp tissue infection (Fig. 5 a). Antibiotic treatment of 2% chlorhexidine digluconate showed perfect suppression of bacterial growth as a positive control. Cu-BGn without or with EGF (10 and 14.5 μg/mL) suppressed bacterial growth over 5 h co-culture while BGn did not display any antibacterial activity, suggesting that the antibacterial effect of Cu-BGn is merely due to released Cu ions.

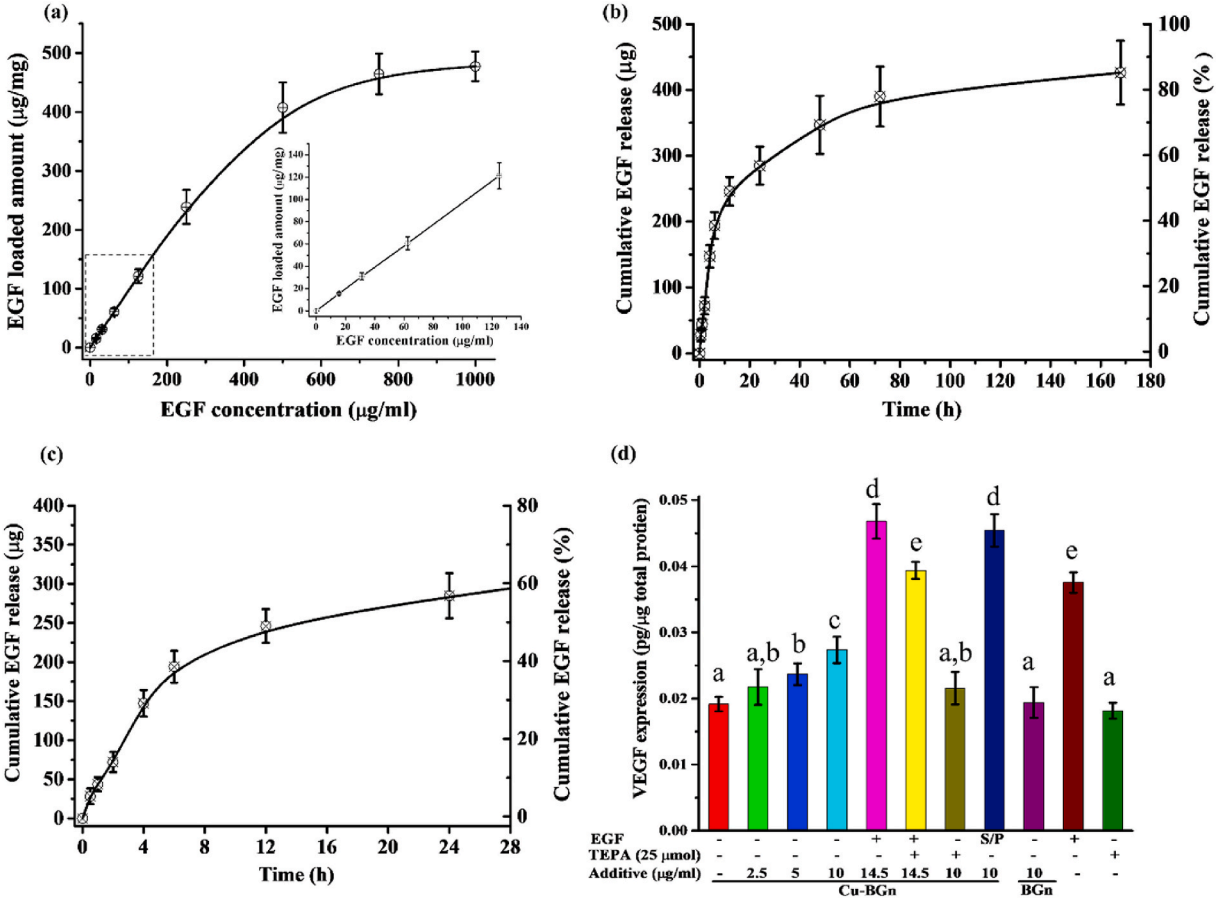

Fig. 4. Loading of epidermal growth factor (EGF) on Cu-BGn (EGF@Cu-BGn), its in-vitro release profile and synergistic VEGF secretion by HUVECs treated with EGF@Cu-BGn nanotherapeutics. For accelerating angiogenesis, various concentrations of EGF (0–1000 μg/mL) were incubated with 1 mg of Cu-BGn for 2 h at 37 °C and loading efficiency was calculated (a); maximally ~450 μg of EGF in 1 mg of Cu-BGn. Long and short-term release (b–c) of EGF from EGF@Cu-BGn complex (1.45 mg) loaded with the maximum amount of EGF per mg of Cu-BGn was gathered in 1 mL of PBS (37 °C) at pre-determined time points up to 7 days. After burst release of EGF biomolecules (~60%) within 24 h, sustained release occurred until 7 days. Synergistic VEGF secretion effects from HUVECs treated with EGF@Cu-BGn nanotherapeutics (d). To determine the efficacy of the EGF@Cu-BGn complex, VEGF secretion from HUVECs into media during 24 h was calculated using VEGF ELISA kit (n = 3). Synergistic increase of VEGF secretion was significantly detected in EGF@Cu-BGn group compared to EGF and Cu-BGn control groups. To verify the angiogenic role of copper ions, 25 μM of TEPA, chelating free copper, was co-treated with nanospheres, displaying significant decrease of VEGF secretion in TEPA treated groups compared to each counterpart. Letters (a, b, c, d and e) indicate significant differences among the groups at $p < 0.05$.

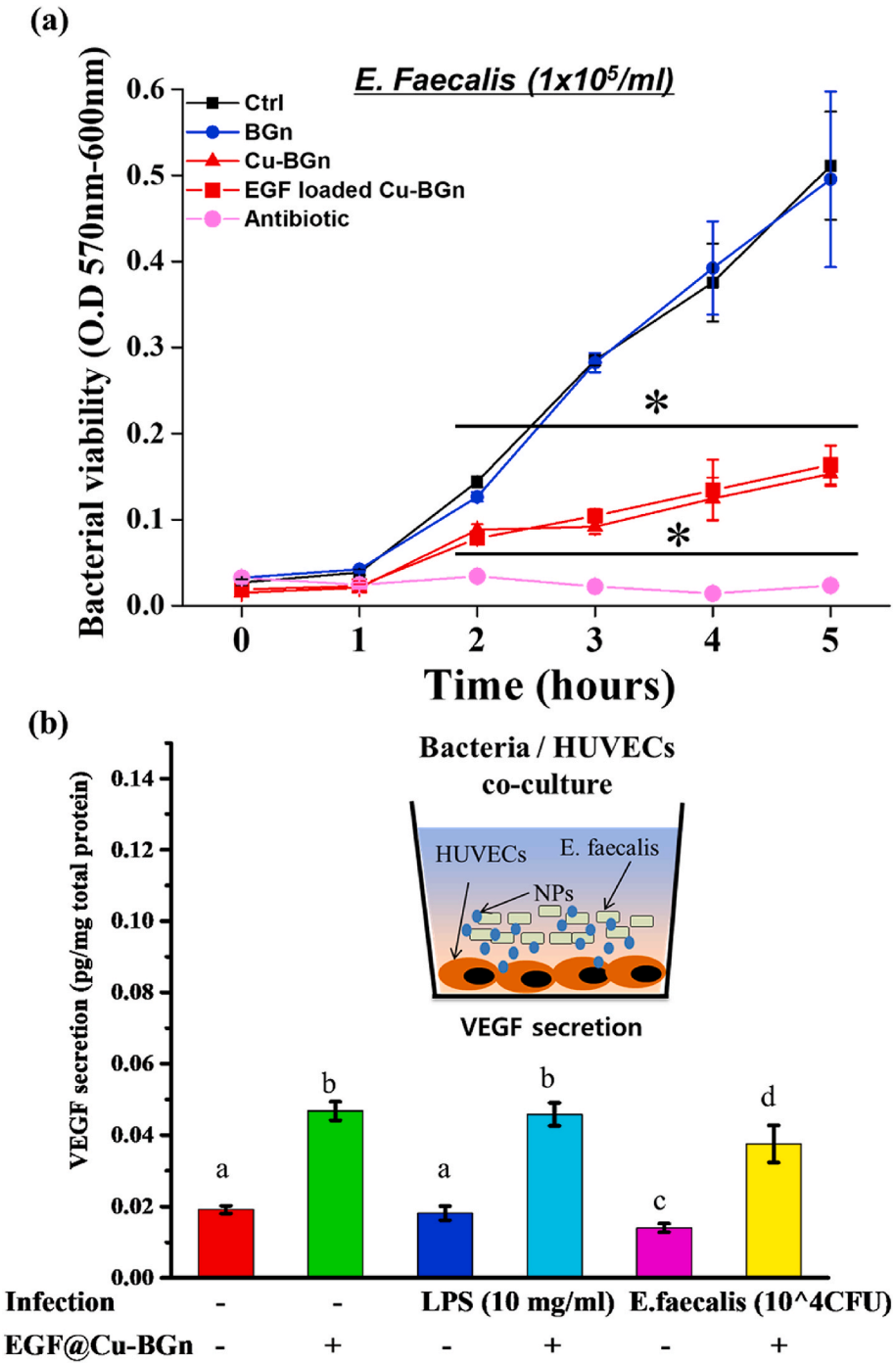

Fig. 5. In vitro antibacterial effects of EGF@Cu-BGn nanotherapeutics on *E. faecalis*. Viability of *E. faecalis* (a) was analyzed by PrestoBlue, and the result showed that the Cu-BGn and EGF@Cu-BGn groups effectively suppressed the bacterial growth (n = 3). Treatment with antibiotic chlorhexidine digluconate was used as a positive control (*: compared to control, $p < 0.05$, n = 4). VEGF secretion, a key blood vessel forming secretome, from HUVECs treated with EGF@Cu-BGn nanotherapeutics (14.5 μg/mL) under inflamed condition (b): LPS (10 μg/mL) or *Enterococcus faecalis* (*E. faecalis*, 10^4 CFU/mL) co-culture. VEGF secretion from inflamed HUVECs was quantified in the conditioning media after 12 h (insert of a schematic image, n = 3). *E. faecalis* co-culture significantly diminished VEGF production while adding EGF@Cu-BGn nanotherapeutics to cell-bacteria co-culture condition recovered VEGF secretion, but slightly decreased the amount compared to EGF@Cu-BGn only treatment group. Letters (a, b, c and d) indicate significant differences among the groups at $p < 0.05$.

Next, HUVECs were cultured with the EGF@Cu-BGn along with simultaneous contamination with E. Faecalis (10^4 CFU/mL) in order to evaluate the multi-functionality of Cu-BGn under a clinically relevant circumstance (Fig. 5 b). *E. faecalis* co-culture significantly diminished VEGF, a key blood vessel forming secretome, production ($P < 0.05$) while adding EGF@Cu-BGn to cell-bacteria co-culture condition recovered VEGF secretion, but slightly decreased the amount compared to EGF@Cu-BGn only treatment group possibly due to toxicity of body of *E. faecalis* after interaction with EGF@Cu-BGn ($P < 0.05$). In an inflammation-induced condition with LPS (10 μg/mL), no significant change of VEGF secretion was observed in HUVECs culture, whereas EGF@Cu-BGn upregulated VEGF secretion compared to control. In the healing process of the infected pulp tissue, the dental pulp tissue naturally increases local blood flow by dilatation of existing blood vessels and the stimulation of new vessel formation in order to eliminate the bacteria species with recruited immune cells [74]. Since the delay of pathogens clearance can compromise angiogenesis of the infected tissue by accumulated toxins and following severe damage, protecting tissue angiogenesis from infection is considered a key idea of therapeutic strategy [75]. In this regard, the co-culture of bacteria/endothelial cells with therapeutic biomaterials or molecules has recently been adopted to mimic the tissue environment which is associated with clinically relevant bacterial infections [48,76–79]. Collectively, EGF@Cu-BGn offered several merits including (1) anti-bacterial effects against a major pulp tissue pathogenic bacterial strain (*E. faecalis*); (2) in-vitro stimulation of angiogenesis and VEGF production in infected HUVEC culture; (3) in vivo osteo/odontogenic regenerative potential of the infected pulp tissue. Such merits of EGF@Cu-BGn

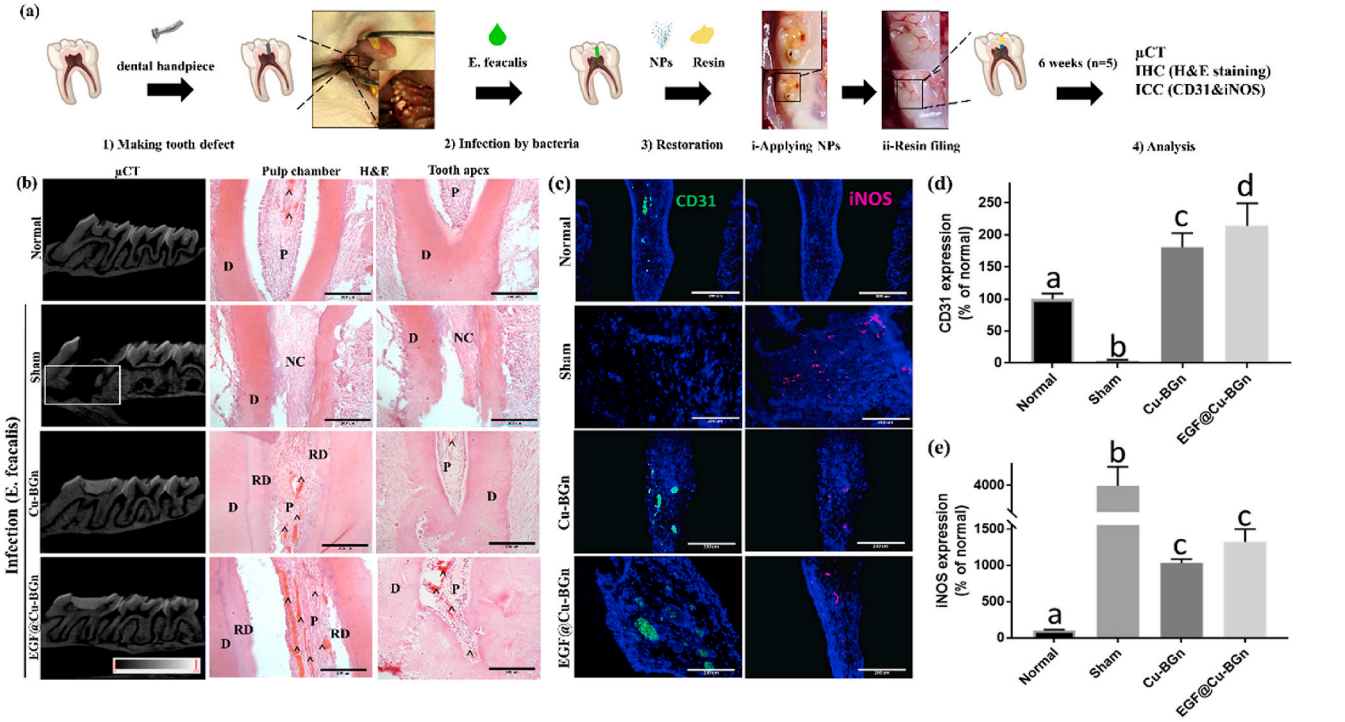

Fig. 6. In vivo efficacy of the EGF@Cu-BGn nanotherapeutics for treatment and regeneration of infected/damaged dental pulp. Schematic illustration and optical photos showing the dental surgery procedure and nanotherapeutics application process in the molar tooth of rat (a). Rat molar teeth (infected with E. feacalis and filled with nanospheres) were scanned by μCT at 6 weeks (b). Destruction of alveolar bone surrounding tooth roots only appeared in the sham operation-infection group (white box) while Cu-BGn and EGF@Cu-BGn groups preserved anatomical structures. Histological analysis by H&E staining (b) revealed the regeneration of tissue complex such as pulp and osteodentin in the pulp chamber; decalcified dentin (D), relatively normal pulp tissues (P), necrotic soft tissues consisting of adipose granules or lymphocytes in the pulp regions (NC), acellular reparative dentin structure (RD), and blood vessels in pulp chamber. NC was only detected in the sham operation-infection group while NPs treatment groups displayed RD and P with abundant blood vessels, markers of regenerative dental pulp from infection. Scale bar: 200 μm. Synergistic neovascularization and inflammation were further investigated by immunohistochemistry (c–e). CD31-positive cells (CD31-FITC) and iNOS-positive cells (iNOS-Rhodamine) were utilized for detecting neovascularization and inflammation during infected dental pulp regeneration. EGF@Cu-BGn treated group showed more CD31 + cells than Cu-BGn counterpart while sham group with bacterial infection totally diminished expression of CD31 + cells, disclosing synergistic angiogenic effects from EGF and Cu^{2+} ions under infected conditions (d). In case of iNOS + cells, Cu-BGn and EGF@Cu-BGn revealed comparably lower (4-fold down) iNOS level than sham infection group, showing anti-inflammatory contribution of Cu^{2+} ions from their anti-bacterial effects (e). Letters (a, b, c and d) indicate significant differences among the groups at $p < 0.05$ ($n = 5$).

potentiate its application for the regeneration of infected bone or dental tissues.

3.7. In vivo regeneration of infected pulp tissue defect

To further investigate the multifunctional and synergistic effect of EGF@Cu-BGn in angiogenesis (EGF and Cu^{2+} ions) and anti-bacterial activity (Cu^{2+} ions) for in vivo regeneration of infected/damaged tissue, EGF@Cu-BGn nanotherapeutics were applied to bacteria-infected rat teeth (Fig. 6 b). We mimicked a clinical dental pulp infection environment using *E. faecalis*, as used in the aforementioned in vitro experiments. *E. faecalis* was administrated to exposed dental pulp followed by EGF@Cu-BGn nanotherapeutics application to the infected defect site. EGF@Cu-BGn nanotherapeutics were applied in touch with dental pulp tissues and possibly interacted with endothelial cells and hMSCs where EGF and ions (Cu^{2+}, Ca^{2+} and SiO_4^{4-}) are released to exert their therapeutic actions on the infected/damaged tissues. After six weeks' post-operation, μ-CT scanning and H&E histological analysis (Fig. 6 c) were performed to observe preservation of the bone around the teeth (which can degrade in a pulp tissue inflammation state). The regenerative microenvironment in the dental pulp tissue obviously contained acellular reparative dentin (RD) and blood vessels (Fig. 6c). Furthermore, well preserved bone around the teeth (as an indicator of successful anti-bacterial therapy) and deposition of regenerative dentin (as a histological marker of pulp regeneration under inflammation) were observed in EGF@Cu-BGn and Cu-BGn groups. In the case of sham-operation with *E. faecalis* infection, destruction of the bone surrounding tooth roots (white box) and severe necrosis of the adjacent soft tissues with adipose granules or lymphocytes (NC) were detected. In addition, EGF@Cu-BGn and Cu-BGn groups were found to contain blood vessels, contrary to the sham group which showed the absence of blood vessels. Interestingly, larger areas of blood vessels were detected in the EGF@Cu-BGn group than the Cu-BGn group as can be seen from H&E images, demonstrating in vivo synergistic angiogenic effect from Cu^{2+} and EGF. In addition, synergistic neovascularization (measured by the number of CD31-positive cells) and inflammation (measured by the number of iNOS-positive cells) were further investigated by immunohistochemistry (CD31-FITC and iNOS-Rhodamine). EGF@Cu-BGn-treated group showed more CD31-positive cells than Cu-BGn counterpart while sham group with bacterial infection had little expression of CD31-positive cells, demonstrating synergistic angiogenic effects from EGF and Cu^{2+} under infected conditions (Fig. 6 c-e). In case of iNOS-positive cells, Cu-BGn and EGF@Cu-BGn revealed lower (4-fold down) iNOS levels than sham control group, showing the bacteria-induced inflammation was subsidized (Fig. 6e).

Taken together, the therapeutic effects of the EGF@Cu-BGn nano-delivery system was proven in terms of pro-angiogenesis (stimulated by release of EGF/Cu^{2+}) and antibacterial activity (induced by Cu^{2+}) in rat infected teeth model, which ultimately effective in improving the regeneration of infected tissue. Lastly, the nanotherapeutic events are schematically shown in Fig. 7 which illustrates the triple-functionality (angiogenic, odontogenic and antibacterial) of the Cu-incorporated/

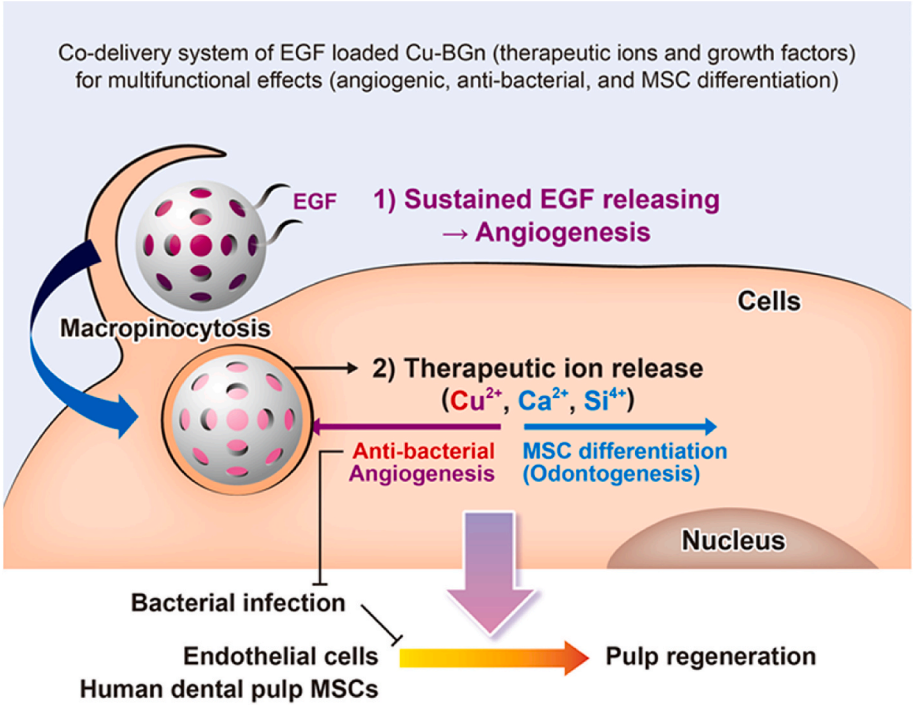

Fig. 7. Triple-functional (pro-angiogenic, anti-bacterial and odontogenic) nanotherapeutics of copper doped/EGF loaded mesoporous bioactive glass nanospheres (Cu-BGn) to regenerate bacterial infected dental pulp. EGF loaded Cu-BGn release EGF biomolecules and Cu^{2+} ions for synergistically enhancing angiogenesis before and after cell-internalization via macropinocytosis. In addition to the role of Cu^{2+} ions in inhibiting bacterial infection, the released bioactive ions (calcium and silicate) could add to stimulating dental pulp MSC differentiation to odontoblast and ultimately for pulp regeneration.

EGF-loaded mesoporous bioactive glass nanospheres in the regeneration of bacterial infected dental pulp.

4. Conclusions

A new nanotherapeutic approach was demonstrated for the regeneration of infected dental pulp tissue defect, where antibacterial, angiogenic and odontogenic effects were combined through the delivery of multiple ions/growth factor (Cu^{2+}/EGF) from mesoporous bioactive glass nanospheres. The release of Cu^{2+} (incorporated into Cu-BGn structure) and EGF (loaded into pores of Cu-BGn) showed a strong antibacterial activity against *E. faecalis* while stimulating angiogenesis of endothelial cells. Moreover, the release of other ions (silicate and calcium) could add to the stimulation of osteo/odontogenesis of MSCs. The in vivo implantation of the EGF@Cu-BGn nanotherapeutics in infected rat molar teeth demonstrated potentially regenerated indication of the infected pulp defect.

CRediT authorship contribution statement

Ahmed El-Fiqi: Conceptualization, Methodology, Data curation, Formal analysis, Writing - original draft. **Nandin Mandakhbayar:** Methodology, Data curation, Formal analysis, Writing - review & editing. **Seung Bin Jo:** Validation, Writing - review & editing. **Jonathan C. Knowles:** Writing - review & editing. **Jung-Hwan Lee:** Conceptualization, Methodology, Data curation, Writing - review & editing, Supervision. **Hae-Won Kim:** Conceptualization, Writing - review & editing, Supervision, Funding acquisition.

Declaration of competing interest

The authors declare no conflict of interests.

Acknowledgment

This work was supported by a National Research Foundation of Korea (NRF) grant funded by the Ministry of Science and ICT (2019R1C1C1002490, 2018R1A2B3003446), by the Global Research Development Center Program (2018K1A4A3A01064257) and by the Priority Research Center Program provided by the Ministry of Education (2019R1A6A1A11034536). The present research was also supported by the research fund of Dankook University for the 2019 University Innovation Support Program.

Appendix A. Supplementary data

Supplementary data to this article can be found online at https://doi.org/10.1016/j.bioactmat.2020.07.010.

References

[1] M.P. Soares, L. Teixeira, L.F. Moita, Disease tolerance and immunity in host protection against infection, Nat. Rev. Immunol. 17 (2) (2017) 83–96.
[2] M. Karin, H. Clevers, Reparative inflammation takes charge of tissue regeneration, Nature 529 (7586) (2016) 307–315.
[3] L.M. Baddour, Y.-M. Cha, W.R. Wilson, Infections of cardiovascular implantable electronic Devices, N. Engl. J. Med. 367 (9) (2012) 842–849.
[4] R.K. Singh, J.C. Knowles, H.-W. Kim, Advances in nanoparticle development for improved therapeutics delivery: nanoscale topographical aspect, J. Tissue Eng. 10 (2019) 2041731419877528-2041731419877528.
[5] M. Kearney, P.R. Cooper, A.J. Smith, H.F. Duncan, Epigenetic approaches to the treatment of dental pulp inflammation and repair: opportunities and obstacles, Front. Genet. 9 (2018) 311.
[6] C. Jung, S. Kim, T. Sun, Y.-B. Cho, M. Song, Pulp-dentin regeneration: current approaches and challenges, J. Tissue Eng. 10 (2019) 2041731418819263-2041731418819263.
[7] J.-C. Farges, B. Alliot-Licht, E. Renard, M. Ducret, A. Gaudin, A.J. Smith, P.R. Cooper, Dental pulp defence and repair mechanisms in dental caries, Mediat. Inflamm. 2015 (2015) 1–16.
[8] I.N. Rôças, J.F. Siqueira Jr., Frequency and levels of candidate endodontic pathogens in acute apical abscesses as compared to asymptomatic apical periodontitis, PloS One 13 (1) (2018) e0190469-e0190469.
[9] T.J. Hilton, Keys to clinical success with pulp capping: a review of the literature, Operat. Dent. 34 (5) (2009) 615–625.
[10] Y. Jiao, F.R. Tay, L.-N. Niu, J.-H. Chen, Advancing antimicrobial strategies for managing oral biofilm infections, Int. J. Oral Sci. 11 (3) (2019) 28-28.
[11] C.P. Endodontics, Part 4 Morphology of the root canal system, Br. Dent. J. 197 (7) (2004) 379–383.
[12] A.C. Anderson, E. Hellwig, R. Vespermann, A. Wittmer, M. Schmid, L. Karygianni, A. Al-Ahmad, Comprehensive analysis of secondary dental root canal infections: a combination of culture and culture-independent approaches reveals new insights, PloS One 7 (11) (2012) e49576-e49576.
[13] V. Miguez-Pacheco, L.L. Hench, A.R. Boccaccini, Bioactive glasses beyond bone and teeth: emerging applications in contact with soft tissues, Acta Biomater. 13 (2015)

1–15.
[14] L. Hench, Bioglass: 10 milestones from concept to commerce, J. Non-Cryst. Solids 432 (2015).
[15] E. O'Neill, G. Awale, L. Daneshmandi, O. Umerah, K.W.H. Lo, The roles of ions on bone regeneration, Drug Discov. Today 23 (4) (2018) 879–890.
[16] A. El-Fiqi, T.-H. Kim, M. Kim, M. Eltohamy, J.-E. Won, E.-J. Lee, H.-W. Kim, Capacity of mesoporous bioactive glass nanoparticles to deliver therapeutic molecules, Nanoscale 4 (23) (2012) 7475–7488.
[17] A. El-Fiqi, J.-H. Kim, H.-W. Kim, Osteoinductive fibrous scaffolds of biopolymer/mesoporous bioactive glass nanocarriers with excellent bioactivity and long-term delivery of osteogenic drug, ACS Appl. Mater. Interfaces 7 (2) (2015) 1140–1152.
[18] B. Sui, G. Zhong, J. Sun, Drug-loadable mesoporous bioactive glass nanospheres: biodistribution, clearance, BRL cellular location and systemic risk assessment via 45Ca labelling and histological analysis, Sci. Rep. 6 (1) (2016) 33443.
[19] T.-H. Kim, R.K. Singh, M.S. Kang, J.-H. Kim, H.-W. Kim, Inhibition of osteoclastogenesis through siRNA delivery with tunable mesoporous bioactive nanocarriers, Acta Biomater. 29 (2016) 352–364.
[20] B. Sui, X. Liu, J. Sun, Dual-functional dendritic mesoporous bioactive glass nanospheres for calcium influx-mediated specific tumor suppression and controlled drug delivery in vivo, ACS Appl. Mater. Interfaces 10 (28) (2018) 23548–23559.
[21] J.-H. Lee, N. Mandakhbayar, A. El-Fiqi, H.-W. Kim, Intracellular co-delivery of Sr ion and phenamil drug through mesoporous bioglass nanocarriers synergizes BMP signaling and tissue mineralization, Acta Biomater. 60 (2017) 93–108.
[22] J.-H. Lee, A. El-Fiqi, N. Mandakhbayar, H.-H. Lee, H.-W. Kim, Drug/ion co-delivery multi-functional nanocarrier to regenerate infected tissue defect, Biomaterials 142 (2017) 62–76.
[23] C.H. Kong, C. Steffi, Z. Shi, W. Wang, Development of mesoporous bioactive glass nanoparticles and its use in bone tissue engineering, J. Biomed. Mater. Res. B Appl. Biomater. 106 (8) (2018) 2878–2887.
[24] Q. Nawaz, M.A.U. Rehman, A. Burkovski, J. Schmidt, A.M. Beltrán, A. Shahid, N.K. Alber, W. Peukert, A.R. Boccaccini, Synthesis and characterization of manganese containing mesoporous bioactive glass nanoparticles for biomedical applications, J. Mater. Sci. Mater. Med. 29 (5) (2018) 64.
[25] Z. Tabia, K. El Mabrouk, M. Bricha, K. Nouneh, Mesoporous bioactive glass nanoparticles doped with magnesium: drug delivery and acellular in vitro bioactivity, RSC Adv. 9 (22) (2019) 12232–12246.
[26] C. Mahapatra, R.K. Singh, J.-J. Kim, K.D. Patel, R.A. Perez, J.-H. Jang, H.-W. Kim, Osteopromoting reservoir of stem cells: bioactive mesoporous nanocarrier/collagen gel through slow-releasing FGF18 and the activated BMP signaling, ACS Appl. Mater. Interfaces 8 (41) (2016) 27573–27584.
[27] K. Zheng, J. Kang, B. Rutkowski, M. Gawęda, J. Zhang, Y. Wang, N. Founier, M. Sitarz, N. Taccardi, A.R. Boccaccini, Toward highly dispersed mesoporous bioactive glass nanoparticles with high Cu concentration using Cu/ascorbic acid complex as precursor, Front. Chem. 7 (2019) 497.
[28] J.-J. Kim, A. El-Fiqi, H.-W. Kim, Synergetic cues of bioactive nanoparticles and nanofibrous structure in bone scaffolds to stimulate osteogenesis and angiogenesis, ACS Appl. Mater. Interfaces 9 (3) (2017) 2059–2073.
[29] N. Mandakhbayar, A. El-Fiqi, J.-H. Lee, H.-W. Kim, Evaluation of strontium-doped nanobioactive glass cement for dentin–pulp complex regeneration therapy, ACS Biomater. Sci. Eng. 5 (11) (2019) 6117–6126.
[30] M. Yu, Y. Xue, P.X. Ma, C. Mao, B. Lei, Intrinsic ultrahigh drug/miRNA loading capacity of biodegradable bioactive glass nanoparticles toward highly efficient pharmaceutical delivery, ACS Appl. Mater. Interfaces 9 (10) (2017) 8460–8470.
[31] T.M. Gross, J. Lahiri, A. Golas, J. Luo, F. Verrier, J.L. Kurzejewski, D.E. Baker, J. Wang, P.F. Novak, M.J. Snyder, Copper-containing glass ceramic with high antimicrobial efficacy, Nat. Commun. 10 (1) (2019) 1979-1979.
[32] J. Zhang, H. Wu, F. He, T. Wu, L. Zhou, J. Ye, Concentration-dependent osteogenic and angiogenic biological performances of calcium phosphate cement modified with copper ions, Mater. Sci. Eng. C 99 (2019) 1199–1212.
[33] L. Weng, S.K. Boda, M.J. Teusink, F.D. Shuler, X. Li, J. Xie, Binary doping of strontium and copper enhancing osteogenesis and angiogenesis of bioactive glass nanofibers while suppressing osteoclast activity, ACS Appl. Mater. Interfaces 9 (29) (2017) 24484–24496.
[34] Y. Zhou, S. Han, L. Xiao, P. Han, S. Wang, J. He, J. Chang, C. Wu, Y. Xiao, Accelerated host angiogenesis and immune responses by ion release from mesoporous bioactive glass, J. Mater. Chem. B Mater. Biol. Med. 6 (20) (2018) 3274–3284.
[35] H. Hu, Y. Tang, L. Pang, C. Lin, W. Huang, D. Wang, W. Jia, Angiogenesis and full-thickness wound healing efficiency of a copper-doped borate bioactive glass/poly (lactic-co-glycolic acid) dressing loaded with vitamin E in vivo and in vitro, ACS Appl. Mater. Interfaces 10 (27) (2018) 22939–22950.
[36] E.J. Ryan, A.J. Ryan, A. González-Vázquez, A. Philippart, F.E. Ciraldo, C. Hobbs, V. Nicolosi, A.R. Boccaccini, C.J. Kearney, F.J. O'Brien, Collagen scaffolds functionalised with copper-eluting bioactive glass reduce infection and enhance osteogenesis and angiogenesis both in vitro and in vivo, Biomaterials 197 (2019) 405–416.
[37] S. Kargozar, F. Baino, S. Hamzehlou, R.G. Hill, M. Mozafari, Bioactive glasses: sprouting angiogenesis in tissue engineering, Trends Biotechnol. 36 (4) (2018) 430–444.
[38] L.B. Romero-Sánchez, M. Marí-Beffa, P. Carrillo, M.Á. Medina, A. Díaz-Cuenca, Copper-containing mesoporous bioactive glass promotes angiogenesis in an in vivo zebrafish model, Acta Biomater. 68 (2018) 272–285.
[39] P.S. Briquez, L.E. Clegg, M.M. Martino, F.M. Gabhann, J.A. Hubbell, Design principles for therapeutic angiogenic materials, Nat. Rev. Mater. 1 (1) (2016) 15006.
[40] M.P. Stelling, J.M. Motta, M. Mashid, W.E. Johnson, M.S. Pavão, N.P. Farrell, Metal ions and the extracellular matrix in tumor migration, FEBS J. 286 (15) (2019) 2950–2964.
[41] H. Rupp, U. Weser, X-ray photoelectron spectroscopy of copper(II), copper(I), and mixed valence systems, Bioinorg. Chem. 6 (1) (1976) 45–59.
[42] K. Dashnyam, A. El-Fiqi, J.O. Buitrago, R.A. Perez, J.C. Knowles, H.-W. Kim, A mini review focused on the proangiogenic role of silicate ions released from silicon-containing biomaterials, J. Tissue Eng. 8 (2017) 2041731417707339-2041731417707339.
[43] J.V. Rau, M. Curcio, M.G. Raucci, K. Barbaro, I. Fasolino, R. Teghil, L. Ambrosio, A. De Bonis, A.R. Boccaccini, Cu-releasing bioactive glass coatings and their in vitro properties, ACS Appl. Mater. Interfaces 11 (6) (2019) 5812–5820.
[44] D. Zepeda-Orozco, H.M. Wen, B.A. Hamilton, N.S. Raikwar, C.P. Thomas, EGF regulation of proximal tubule cell proliferation and VEGF-A secretion, Phys. Rep. 5 (18) (2017) e13453.
[45] Z. Wang, Z. Wang, W.W. Lu, W. Zhen, D. Yang, S. Peng, Novel biomaterial strategies for controlled growth factor delivery for biomedical applications, NPG Asia Mater. 9 (10) (2017) e435-e435.
[46] M.R. Schneider, M. Sibilia, R.G. Erben, The EGFR network in bone biology and pathology, Trends Endocrinol. Metabol. 20 (10) (2009) 517–524.
[47] J.-H. Lee, M.-S. Kang, C. Mahapatra, H.-W. Kim, Effect of aminated mesoporous bioactive glass nanoparticles on the differentiation of dental pulp stem cells, PloS One 11 (3) (2016) e0150727-e0150727.
[48] S. Zaatreh, K. Wegner, M. Strauß, J. Pasold, W. Mittelmeier, A. Podbielski, B. Kreikemeyer, R. Bader, Co-culture of S. Epidermidis and human osteoblasts on implant surfaces: an advanced in vitro model for implant-associated infections, PloS One 11 (3) (2016) e0151534-e0151534.
[49] F. Li, P. Wang, M.D. Weir, A.F. Fouad, H.H.K. Xu, Evaluation of antibacterial and remineralizing nanocomposite and adhesive in rat tooth cavity model, Acta Biomater. 10 (6) (2014) 2804–2813.
[50] T. Dammaschke, Rat molar teeth as a study model for direct pulp capping research in dentistry, Lab. Anim. 44 (1) (2010) 1–6.
[51] R. Kayestha, Sumati, K. Hajela, ESR studies on the effect of ionic radii on displacement of Mn2+ bound to a soluble β-galactoside binding hepatic lectin, FEBS Lett. 368 (2) (1995) 285–288.
[52] J. Kaewkhao, S. Rhianphumikarakit, N. Udomkan, ESR and optical absorption spectra of copper (II) ions in glasses, Adv. Mater. Res. 55–57 (2008) 849–852.
[53] M.S. Kim, A. El-Fiqi, J.-W. Kim, H.-S. Ahn, H. Kim, Y.-J. Son, H.-W. Kim, J.K. Hyun, Nanotherapeutics of PTEN inhibitor with mesoporous silica nanocarrier effective for axonal outgrowth of adult neurons, ACS Appl. Mater. Interfaces 8 (29) (2016) 18741–18753.
[54] A. El-Fiqi, J.H. Lee, E.-J. Lee, H.-W. Kim, Collagen hydrogels incorporated with surface-aminated mesoporous nanobioactive glass: improvement of physicochemical stability and mechanical properties is effective for hard tissue engineering, Acta Biomater. 9 (12) (2013) 9508–9521.
[55] S.K. Kundu, A. Kayet, R. Baidya, L. Satyanarayana, D.K. Maiti, Nanofibrils of a CuII-Thiophenyltriazine-Based porous polymer: a diverse heterogeneous nanocatalyst, ACS Omega 5 (1) (2020) 394–405.
[56] Z.A. Alothman, A review: fundamental aspects of silicate mesoporous materials, Materials 5 (12) (2012) 2874–2902.
[57] A. El-Fiqi, J.-H. Kim, H.-W. Kim, Novel bone-mimetic nanohydroxyapatite/collagen porous scaffolds biomimetically mineralized from surface silanized mesoporous nanobioglass/collagen hybrid scaffold: physicochemical, mechanical and in vivo evaluations, Mater. Sci. Eng. C (2020) 110660.
[58] X. Li, X. Wang, D. He, J. Shi, Synthesis and characterization of mesoporous CaO–MO–SiO2–P2O5 (M = Mg, Zn, Cu) bioactive glasses/composites, J. Mater. Chem. 18 (34) (2008) 4103–4109.
[59] A. El-Fiqi, J.O. Buitrago, S.H. Yang, H.-W. Kim, Biomimetically grown apatite spheres from aggregated bioglass nanoparticles with ultrahigh porosity and surface area imply potential drug delivery and cell engineering applications, Acta Biomater. 60 (2017) 38–49.
[60] G.-f. Hu, Copper stimulates proliferation of human endothelial cells under culture, J. Cell. Biochem. 69 (3) (1998) 326–335.
[61] C. Giacomelli, M.L. Trincavelli, C. Satriano, Ф. Hansson, D. La Mendola, E. Rizzarelli, C. Martini, ♦Copper (II) ions modulate Angiogenin activity in human endothelial cells, Int. J. Biochem. Cell Biol. 60 (2015) 185–196.
[62] H.J. Kim, S.J. You, D.H. Yang, J. Eun, H.K. Park, M.S. Kim, H.J. Chun, Injectable hydrogels based on MPEG–PCL–RGD and BMSCs for bone tissue engineering, Biomater. Sci. 8(15) (2020) 4334–4345.
[63] R. El-Gendy, X.B. Yang, P.J. Newby, A.R. Boccaccini, J. Kirkham, Osteogenic differentiation of human dental pulp stromal cells on 45S5 Bioglass® based scaffolds in vitro and in vivo, Tissue Eng. 19 (5–6) (2013) 707–715.
[64] S.-K. Jun, J.-Y. Yoon, C. Mahapatra, J.H. Park, H.-W. Kim, H.-R. Kim, J.-H. Lee, H.-H. Lee, Ceria-incorporated MTA for accelerating odontoblastic differentiation via ROS downregulation, Dent. Mater. 35 (9) (2019) 1291–1299.
[65] X. Zhang, C. Wu, J. Chang, J. Sun, Odontogenic differentiation of human dental pulp cells induced by silicate-based bioceramics via activation of P38/MEPE pathway, RSC Adv. 5 (89) (2015) 72536–72543.
[66] K. Dashnyam, G.-Z. Jin, J.-H. Kim, R. Perez, J.-H. Jang, H.-W. Kim, Promoting angiogenesis with mesoporous microcarriers through a synergistic action of delivered silicon ion and VEGF, Biomaterials 116 (2017) 145–157.
[67] A.A. Ucuzian, A.A. Gassman, A.T. East, H.P. Greisler, Molecular mediators of angiogenesis, J. Burn Care Res. 31 (1) (2010) 158–175.
[68] L. Lamalice, F. Le Boeuf, J. Huot, Endothelial cell migration during angiogenesis, Circ. Res. 100 (6) (2007) 782–794.
[69] C. Wu, Y. Zhou, M. Xu, P. Han, L. Chen, J. Chang, Y. Xiao, Copper-containing mesoporous bioactive glass scaffolds with multifunctional properties of angiogenesis capacity, osteostimulation and antibacterial activity, Biomaterials 34 (2)

(2013) 422–433.
[70] S. Li, H. Xie, S. Li, Y.J. Kang, Copper stimulates growth of human umbilical vein endothelial cells in a vascular endothelial growth factor-independent pathway, Exp. Biol. Med. 237 (1) (2012) 77–82.
[71] C. Gérard, L.-J. Bordeleau, J. Barralet, C.J. Doillon, The stimulation of angiogenesis and collagen deposition by copper, Biomaterials 31 (5) (2010) 824–831.
[72] C. Stähli, M. James-Bhasin, A. Hoppe, A.R. Boccaccini, S.N. Nazhat, Effect of ion release from Cu-doped 45S5 Bioglass® on 3D endothelial cell morphogenesis, Acta Biomater. 19 (2015) 15–22.
[73] C.K. Goldman, J. Kim, W.L. Wong, V. King, T. Brock, G.Y. Gillespie, Epidermal growth factor stimulates vascular endothelial growth factor production by human malignant glioma cells: a model of glioblastoma multiforme pathophysiology, Mol. Biol. Cell 4 (1) (1993) 121–133.
[74] N. Osherov, R. Ben-Ami, Modulation of host angiogenesis as a microbial survival strategy and therapeutic target, PLoS Pathog. 12 (4) (2016) e1005479.
[75] P. Carmeliet, Angiogenesis in life, disease and medicine, Nature 438 (7070) (2005) 932–936.
[76] K. Boldbaatar, K. Dashnyam, J.C. Knowles, H.-H. Lee, J.-H. Lee, H.-W. Kim, Dual-ion delivery for synergistic angiogenesis and bactericidal capacity with silica-based microsphere, Acta Biomater. 83 (2019) 322–333.
[77] D.S. Trentin, D.B. Silva, A.P. Frasson, O. Rzhepishevska, M.V. da Silva, E.d.L. Pulcini, G. James, G.V. Soares, T. Tasca, M. Ramstedt, R.B. Giordani, N.P. Lopes, A.J. Macedo, Natural Green coating inhibits adhesion of clinically important bacteria, Sci. Rep. 5 (2015) 8287-8287.
[78] L. Goers, P. Freemont, K.M. Polizzi, Co-culture systems and technologies: taking synthetic biology to the next level, J. R. Soc. Interface 11 (96) (2014) 20140065.
[79] A. Leyendecker Junior, C.C. Gomes Pinheiro, T. Lazzaretti Fernandes, D. Franco Bueno, The use of human dental pulp stem cells for in vivo bone tissue engineering: a systematic review, J. Tissue Eng. 9 (2018) 2041731417752766-2041731417752766.